Interferometric imaging of nonlocal electromechanical power transduction in ferroelectric domains

Lu Zheng[a,1], Hui Dong[b,1], Xiaoyu Wu[a], Yen-Lin Huang[a], Wenbo Wang[c], Weida Wu (吴伟达)[c], Zheng Wang[b,2], and Keji Lai[a,2]

[a]Department of Physics, University of Texas at Austin, Austin, TX 78712; [b]Department of Electrical and Computer Engineering, University of Texas at Austin, Austin, TX 78712; and [c]Department of Physics and Astronomy, Rutgers University, Piscataway, NJ 08854

Edited by Ramamoorthy Ramesh, University of California, Berkeley, CA, and accepted by Editorial Board Member Zachary Fisk April 11, 2018 (received for review December 27, 2017)

The electrical generation and detection of elastic waves are the foundation for acoustoelectronic and acoustooptic systems. For surface acoustic wave devices, microelectromechanical/nanoelectromechanical systems, and phononic crystals, tailoring the spatial variation of material properties such as piezoelectric and elastic tensors may bring significant improvements to the system performance. Due to the much slower speed of sound than speed of light in solids, it is desirable to study various electroacoustic behaviors at the mesoscopic length scale. In this work, we demonstrate the interferometric imaging of electromechanical power transduction in ferroelectric lithium niobate domain structures by microwave impedance microscopy. In sharp contrast to the traditional standing-wave patterns caused by the superposition of counterpropagating waves, the constructive and destructive fringes in microwave dissipation images exhibit an intriguing one-wavelength periodicity. We show that such unusual interference patterns, which are fundamentally different from the acoustic displacement fields, stem from the nonlocal interaction between electric fields and elastic waves. The results are corroborated by numerical simulations taking into account the sign reversal of piezoelectric tensor in oppositely polarized domains. Our work paves ways to probe nanoscale electroacoustic phenomena in complex structures by near-field electromagnetic imaging.

microwave impedance microscopy | electromechanical power transduction | surface acoustic wave | interference patterns | ferroelectric material

The hallmark of wave interference, a ubiquitous phenomenon in nature, is the appearance of time-independent spatially varying patterns of the oscillation amplitude (1). In the famous Young's double-slit experiment, alternating bright and dark bands on the detector screen vividly demonstrate the wave nature of light, where the periodicity of the interference pattern is proportional to the wavelength. Two counterpropagating waves, one usually generated by boundary-induced reflection of the other, can also interfere with each other to form a standing-wave pattern with a half-wavelength periodicity. In both cases, the interference fringes reveal the hidden phase information of the wave, which enables measurements with superior sensitivity, information capacity (2), and resolution (3) far beyond the wavelength limit. As a result, interferometry has become the basis for nearly all ultraprecision metrology in science and technology, ranging from astronomy (4) and quantum physics (5) to radar (6) and medical imaging (7).

Wave interference is generally caused by the superposition of local oscillating fields of individual waves at each point in the space. In this work, we demonstrate a special type of interference from the superposition of nonlocal interaction between electric fields and elastic waves in ferroelectric domain structures. Because of the sign reversal of piezoelectric tensor in oppositely polarized domains, the fringe patterns in microwave impedance maps are fundamentally different from that of the underlying acoustic fields. Our results are corroborated by first-principle numerical simulations. Microscopy on piezoelectric energy transduction is highly desirable for the design and characterization of novel surface acoustic wave (SAW) devices (8), microwave microelectromechanical/nanoelectromechanical systems (MEMS/NEMS) (9), and phonon–polariton systems (10). In this context, our work may open a research frontier to explore various nanoscale elastic phenomena in these systems by near-field electromagnetic imaging.

The experimental technique in this study is microwave impedance microscopy (MIM) (11), as schematically illustrated in Fig. 1*A*. The excitation signal $V = V_0\, e^{i2\pi ft}$ (voltage V_0 around 0.1 V and frequency f from 100 MHz to 10 GHz) is delivered to the center conductor of a shielded cantilever probe (12). The tip can be viewed as a point voltage source since its diameter at the apex (~100 nm) is much smaller than the acoustic wavelength at these frequencies. The MIM electronics detect the real and imaginary components of the tip–sample admittance $Y = G + iB$ (G, conductance; B, susceptance), which are displayed as MIM-Re and MIM-Im images, respectively (13). The MIM has been widely used for the study of nanoscale permittivity (14) and conductivity (15) distributions in complex systems. In the following, we will show that it can also reveal information on the electroacoustic power transduction in piezoelectric materials.

Significance

The conversion between electrical and acoustic signals in piezoelectric materials is of fundamental importance for their applications. Because of the much slower speed of sound than speed of light in solids, mesoscopic imaging is imperative for the study of electroacoustic behaviors at microwave frequencies. In this paper, the electromechanical power transduction in lithium niobate domains is spatially resolved by microwave impedance microscopy. Because of the sign reversal of piezoelectric tensor in opposite domains, the interaction between electric fields and elastic waves leads to fringe patterns that are fundamentally different from the acoustic displacement fields. This approach uncovers hidden information in the piezoelectric transduction process and opens a frontier to explore various elastic phenomena in materials and devices.

Author contributions: K.L. designed research; L.Z., H.D., X.W., Y.-L.H., W. Wang, and W. Wu performed research; L.Z., H.D., X.W., Y.-L.H., W. Wang, W. Wu, Z.W., and K.L. analyzed data; and Z.W. and K.L. wrote the paper.

The authors declare no conflict of interest.

This article is a PNAS Direct Submission. R.R. is a guest editor invited by the Editorial Board.

[1]L.Z. and H.D. contributed equally to this work.

[2]To whom correspondence may be addressed. Email: zheng.wang@austin.utexas.edu or kejilai@physics.utexas.edu.

This article contains supporting information online at www.pnas.org/lookup/suppl/doi:10.1073/pnas.1722499115/-/DCSupplemental.

Published online May 7, 2018.

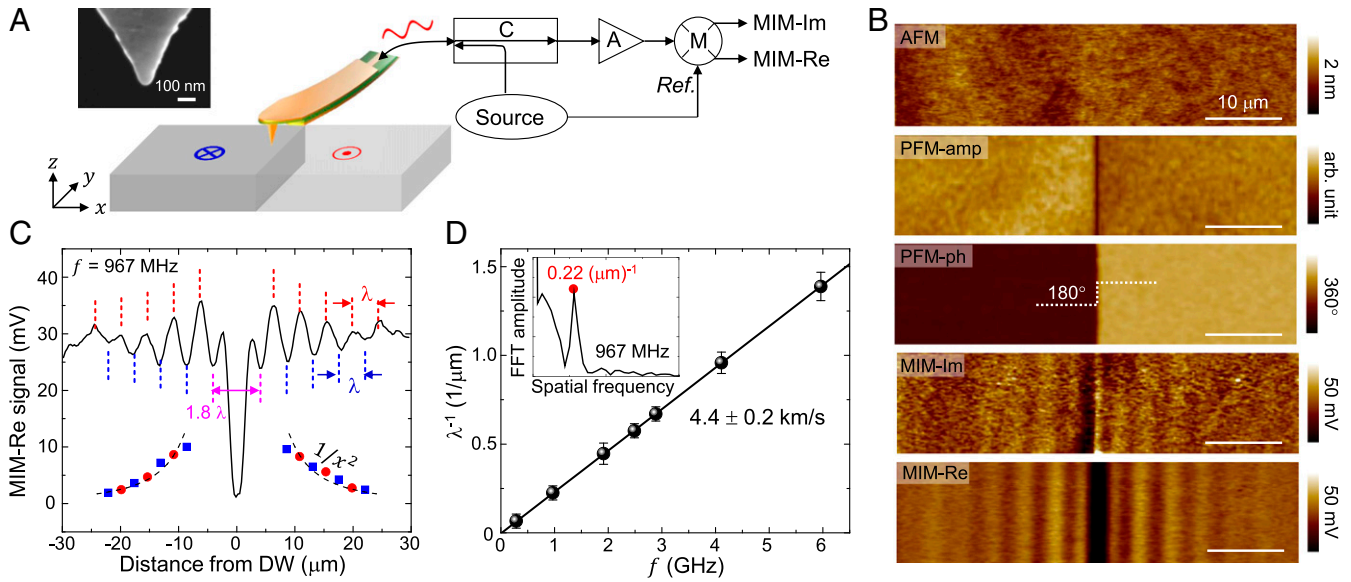

Fig. 1. Microwave imaging around a single $LiNbO_3$ domain wall. (*A*) Schematics of the MIM probe, electronics, and the *z*-cut $LiNbO_3$ sample with a single domain wall. The microwave signal is delivered to the cantilever tip by a directional coupler, and the reflected signal is amplified and mixed with the reference signal to form the MIM-Im and MIM-Re images. (*Inset*) The scanning electron microscopy image of a typical tip apex. (*B*) From top to bottom: AFM, PFM amplitude (PFM-amp), and phase (PFM-ph) images and MIM-Im/Re (f = 967 MHz) images of the sample. (Scale bars, 10 μm.) (*C*) MIM-Re line profile, in which the peaks and valleys are marked by red and blue dashed lines, respectively. Note that the first pair of troughs (labeled by pink dashed lines) are separated by 1.8 λ. The oscillation amplitude at each peak (red circles) and valley (blue squares) is the difference between its signal and the average signal of the two adjacent valleys and peaks, respectively. The black dashed lines are fits to the inverse square of the distance to the wall. (*D*) Linear relation between λ^{-1} and the frequency. The slope corresponds to a wave velocity of 4.4 ± 0.2 km/s. (*Inset*) The Fourier transform of the data in *C* with a spatial frequency of 0.22 $(\mu m)^{-1}$.

Our sample is single-crystalline lithium niobate ($LiNbO_3$), which is technologically important because of its high piezoelectric constants (16), low acoustic attenuation (17, 18), and strong second-order nonlinear optical coefficients (19, 20). $LiNbO_3$ has a trigonal (class 3m) crystal structure with a mirror *yz* plane and a direct triad *z* axis along the polar direction (16). The polarization can be switched by electrical poling (19, 21), allowing artificial domain patterns at micrometer sizes to be created for microwave signal processing (17, 18) and nonlinear optics (19, 20). We start with the simplest scenario around a straight domain wall (DW) on a *z*-cut $LiNbO_3$ sample (Fig. 1*A*). At a first glance, the system is akin to the electron wave interference near an atomic step edge imaged by scanning tunneling microscopy (22). Because the domain inversion flips the sign of odd-rank tensors (the first rank polarization P and the third rank piezoelectric tensor e) (16), the two oppositely polarized domains can be visualized by piezo-force microscopy (PFM) in Fig. 1*B*. The MIM data at f = 967 MHz in the same area are also displayed in Fig. 1*B*. The MIM-Im image, which represents the nondissipative dielectric response, only shows weak contrast possibly due to the static surface charge. The MIM-Re image, on the other hand, exhibits clear interference fringes around the DW. Because the electrical conductance of $LiNbO_3$ due to free carriers is negligible, the MIM-Re contrast indicates that the microwave energy is dissipated through the piezoelectric transduction rather than the Ohmic loss.

Fig. 1*C* shows the averaged MIM-Re line profile across the DW. Neglecting a small spike on the wall due to the dielectric loss associated with DW vibrations (23), the main features include a prominent dip at the DW and damped oscillations with a periodicity of λ away from the wall. Here λ is found to be 4.55 μm from the Fourier transform of the ripples (Fig. 1*D*, *Inset*), and the oscillation amplitude decays quadratically with the distance to the wall. We notice that the first pair of crests only develop as weak shoulders, and the first pair of troughs are separated by 1.8 λ rather than 2 λ. Similar MIM results are observed from 285 MHz to 6 GHz (Fig. S1). As shown in Fig. 1*D*, the measured 1/λ scales linearly with f, and the slope corresponds to an apparent phase velocity of 4.4 ± 0.2 km/s. Comparing it with the velocities of *x*-propagating acoustic waves (18, 24, 25) on *z*-cut $LiNbO_3$ (Table 1), it is clear that the results have the closest match to the pseudo-surface acoustic wave (P-SAW) (26), whose dispersion lies in the continuum of bulk waves. Unlike the Rayleigh SAW (hereafter denoted as SAW) that exists on the surface of all solids (26), this electroacoustic Bleustein–Gulyaev (27, 28) SAW only exists on the surface of piezoelectric materials. The displacement fields of the P-SAW are primarily polarized in the *y* direction (29), although the wave is not purely transverse-horizontal due to the lack of an even-order symmetry axis in $LiNbO_3$.

It is tempting to interpret the MIM-Re fringes as the standing-wave patterns of the acoustic displacement fields underneath the tip, similar to those measured by scanning laser vibrometry (30, 31), scanning electron microscopy (32, 33), and scanning probe microscopy (34, 35). However, should the data represent a standing-wave pattern due to strong reflection off a DW, as suggested by an earlier MIM work (36), the measured periodicity would indicate the dominance of a guided wave with an extraordinarily large phase velocity of 8.8 km/s. In fact, since the acoustic impedance is the same for both domains, the reflection of displacement fields from the *yz* DW is rather weak for both SAW and P-SAW, whereas the associated electric fields change sign across the DW due to the opposite piezoelectric coefficients (Fig. S2). A careful analysis of the tip–sample interaction is therefore necessary to understand the intriguing interference pattern in Fig. 1*B*.

In $LiNbO_3$, the local mechanical strain and electric field are coupled by the piezoelectric effect. As a result, the tip displacement under an AC bias in the PFM measurement can be quantitatively analyzed by 3D finite-element modeling (37, 38).

Table 1. Velocities and properties of the acoustic waves propagating along the *x* axis on *z*-cut $LiNbO_3$ surface

Annotation	Velocity, km/s	Properties	Polarization
Rayleigh surface wave	3.82	Surface guided, nonleaky	*x*- and *z*-dominant
Slow transverse bulk wave	4.08	Bulk continuum	*y*-dominant
Bleustein–Gulyaev pseudo-surface wave	4.55	Surface guided, leaky	*y*-dominant
Fast transverse bulk wave	4.79	Bulk continuum	*z*-dominant
Longitudinal bulk wave	6.55	Bulk continuum	*x*-dominant

The Rayleigh SAW is confined to the surface (nonleaky). The Bleustein–Gulyaev pseudo-SAW has a velocity greater than that of the slow transverse bulk wave. Its energy therefore leaks to the bulk during the propagation.

The MIM, on the other hand, measures the total power dissipation, and numerical simulations have to take into account the energy transduction in the entire sample rather than the local displacement underneath the tip. Here energy conservation dictates that the loss in electrical power $\vec{j}\cdot\vec{E}^*$ (j, current density; E, electric field) is equal to the mechanical power $\vec{F}\cdot\dot{\vec{u}}^*$ (F, electromechanical force density; u, displacement field; $\dot{u}$, time derivative of u), which excites various acoustic waves in solids (26). The electromechanical force can be derived from the divergence of the stress field as $\vec{F}=\text{div}\ T$. Since P-SAW is dominated by the y component of its displacement fields, the power transduction is predominantly determined by the overlap between F_y and $\dot{u}_y$. Using vector calculus, one can show that F_y is symmetric around the tip on a single domain (Fig. S3). To satisfy the continuity condition, $\dot{u}_y$ is also an even function with respect to $x=x_{\text{tip}}$. Because of the sign flip of e across the DW, the overlap integral of $\text{Re}(\int F_y\cdot\dot{u}_y^* dx)$ in the two shaded areas in Fig. 2*A* cancels each other, leading to a drop in power transduction when the tip is close to the wall. As the tip moves away from the DW, the truncated overlap integral within $x\in(0,\ 2x_{\text{tip}})$ oscillates with the same periodicity as $\dot{u}_y$ and shows the power law decrease of amplitude. Here the overlap integral of nonlocal acoustic wave sources are analogous to that in phased array antennas (6), where distributed electromagnetic source configuration and position result in corresponding variations of the antenna impedance. Because the fringe patterns are a result of the interference of nonlocal power transduction rather than the local displacement fields of counterpropagating waves, oscillations in the microwave dissipation can be observed even in the absence of DW reflection. In reality, partial reflection of the SAW and P-SAW displacements always exists at the DW. The fact that only one-wavelength oscillation is visible in Fig. 1*C*, however, indicates that DW reflection is insignificant and does not change the overall picture here.

The qualitative picture above is confirmed by numerical simulations using finite-element analysis (FEA). Due to the prohibitive computational cost of a full 3D modeling for the sample volume exceeding 1,000 λ^3, we truncate the material in the y direction using periodic boundary condition, effectively treating the tip as an infinitely long line source (1 V at 1 GHz) along the y axis (Fig. S4). Except for the fact that the E field decays as $1/r$ from the tip rather than $1/r^2$ in the actual case, this approximation captures the essential physics in our experiment, especially the phase velocities of the acoustic waves. Among the various acoustic waves excited by the tip (Fig. 2*B*), bulk waves do not contribute to periodic oscillations as the tip moves away from the DW. Further analysis (Fig. S5) shows that the power of the P-SAW excited by the tip is ~5 times higher than that of the SAW, supporting our qualitative description above. As seen in Fig. 2*C*, the simulated power dissipation $\text{Re}(\int\vec{j}^*\cdot\vec{E}\ d^3r)$ reproduces major features in the MIM-Re data, including the prominent dip at the DW and the damped oscillations with 1-λ periodicity. The use of a line source in the modeling is responsible for the $1/x$ rather than $1/x^2$ decay of the oscillation amplitude. The reduced separation between the first pair of troughs, 1.8 λ rather than 2 λ, is also seen in the FEA result. We speculate that the deviation is due to DW reflection being no longer negligible when the tip–wall distance is less than one wavelength, although further work is needed to understand this behavior.

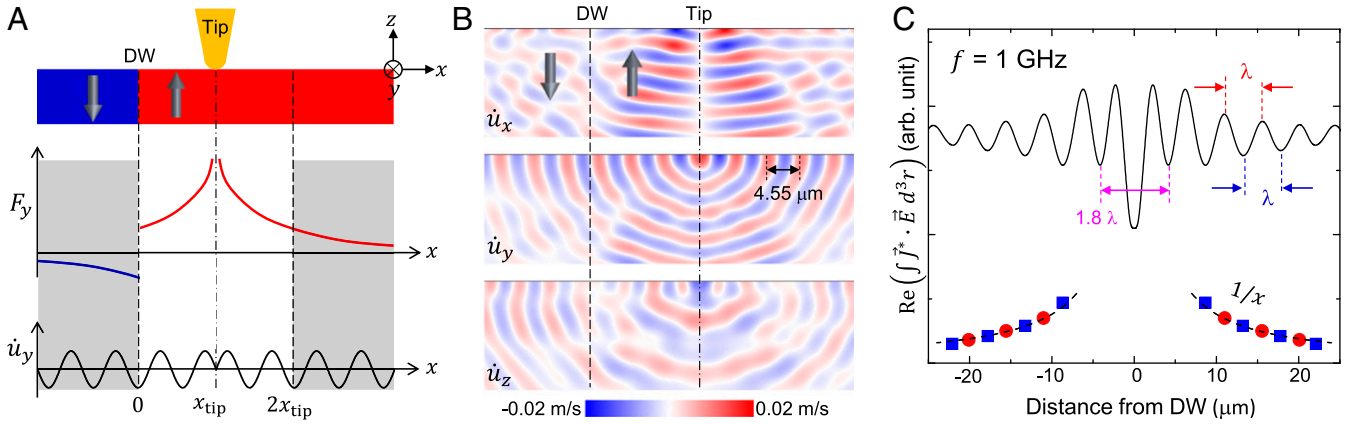

Fig. 2. Numerical simulation of the power transduction near a single domain wall. (*A*) (*Top*) Schematic view of the tip–sample configuration in the *xz* plane. (*Middle*) Sketches of the *y* components of the mechanical force and (*Bottom*) time derivative of the displacement near the surface. The sign of F_y is flipped in opposite domains due to the sign reversal of piezoelectric coefficients. The overlap integral of $F_y\cdot\dot{u}_y$ in the two shaded areas cancels each other. (*B*) Snapshots of the (*Top*) *x*, (*Middle*) *y*, and (*Bottom*) *z* components of the simulated time derivative of displacement fields in the *xz* plane. The P-SAW with a wavelength of 4.55 μm at 1 GHz is seen in the *y* component of the velocity fields. (*C*) Numerical simulation of the dissipated electrical power as a function of the tip position. The strength of the oscillation amplitude scales with $1/x$ (dashed lines) instead of $1/x^2$ from the wall due to the use of a line source in the modeling.

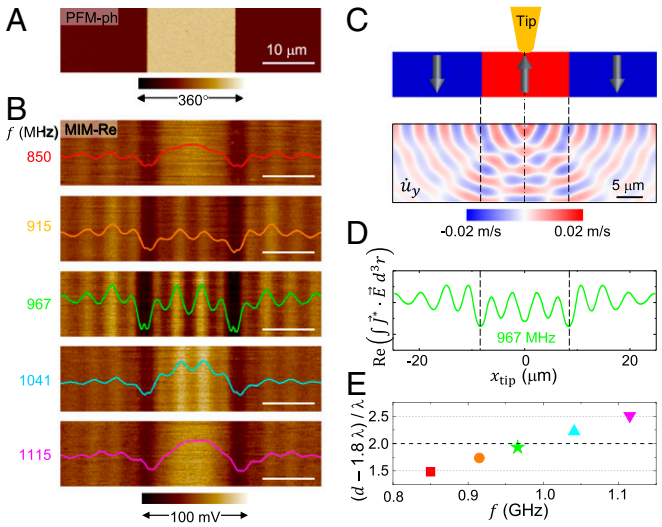

Fig. 3. Imaging and simulation of the double-DW sample. (*A*) Out-of-plane PFM phase image of the double-DW sample. (*B*) MIM-Re images and the corresponding line profiles at five different frequencies. (Scale bars, 10 μm.) (*C*) (*Top*) Tip–sample configuration and (*Bottom*) simulated $\dot{u}_y$ field at 967 MHz of the double-DW sample. (*D*) Simulated electrical power dissipation as a function of the tip position. The two dashed lines indicate the locations of the two walls. (*E*) $(d - 1.8\,\lambda)/\lambda$ as a function of *f*. The five frequency points, which are color coded the same as that in *B*, are selected such that $(d - 1.8\,\lambda)$ roughly equals 1.5 λ, 1.75 λ, 2.0 λ, 2.25 λ, and 2.5 λ.

We now move on to the $LiNbO_3$ sample with two parallel DWs (PFM image in Fig. 3*A*). The corresponding MIM-Re images at five different frequencies are shown in Fig. 3*B*. The strength of the fringes increases as *f* goes from 850 MHz to 967 MHz and decreases as *f* further increases toward 1,115 MHz. Fig. 3 *C* and *D* display the simulated acoustic fields and microwave power loss at $f = 967$ MHz. As summarized in Fig. 3*E*, when the DW spacing *d* covers the distance between the first pair of troughs (~1.8 λ) and an integer multiple of the wavelength, e.g., $d \sim 1.8\,\lambda + 2\,\lambda$ at $f = 967$ MHz, the two sets of ripples centered around the DWs reinforce each other, resulting in stronger peak-to-valley contrast. On the contrary, when $d - 1.8\,\lambda \sim 2 \pm 0.5\,\lambda$ at 850 MHz and 1,115 MHz, the two sets of ripples are opposite in phase by 180°, resulting in suppressed oscillation strengths. More importantly, the ripples remain strong outside the two DWs at $f = 967$ MHz, which is direct evidence of the nonlocal power transduction nature of the MIM-Re images. If the data represent the standing-wave amplitude of the acoustic displacement fields (36), this on-resonance–like image should be free of oscillations outside the double-DW because a Fabry–Perot interferometer does not reflect on resonance (1). In addition, the fringes in Fig. 3*B* exhibit periodicity identical to the wavelength of the underlying acoustic wave, whereas the standing-wave patterns in a Fabry–Perot interferometer have a periodicity of half-λ.

Finally, we present the MIM results on several closed domain structures. Fig. 4 *A*–*D* show the PFM and MIM-Re images (complete data in Fig. S6) of four corral domains shaped in an equilateral triangle, a hexagon, a circle, and a square, respectively. Because of the crystal symmetry (16), DWs on the *z*-cut $LiNbO_3$ surface can only form straight lines along the three *y*-equivalent axes and become curved in other directions. Consequently, the domain designed to be a circle (Fig. 4*C*) appears as a rounded hexagon after electrical poling, and the domain designed to be a square (Fig. 4*D*) appears as a distorted rectangle. Beautiful interference patterns due to the superposition of ripples around each DW are observed in the MIM-Re images. For instance, the rectangular-lattice–like pattern in Fig. 4*D* can be viewed as an overlay of two sets of oscillations parallel to the *x* axis and *y* axis. The different velocities of P-SAW along the two directions (39), as calculated from the FEA (Fig. 4*E*), manifest in

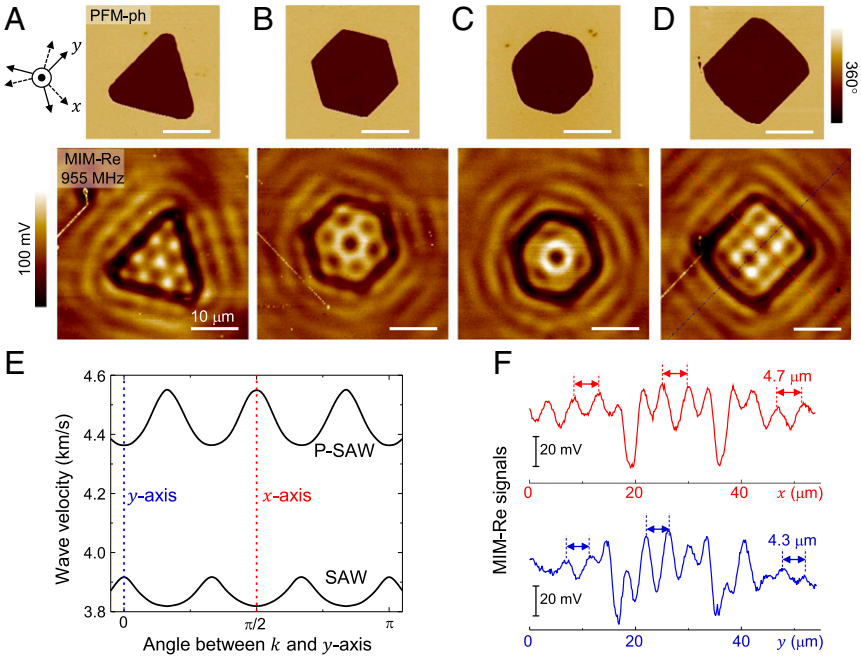

Fig. 4. Interference of piezoelectric transduction in corral domains. (*A*–*D*) (*Top*) PFM-ph and (*Bottom*) MIM-Re images at $f = 955$ MHz of four closed $LiNbO_3$ domains. Clear interference patterns due to the superposition of ripples around each DW are seen in the MIM-Re data. (Scale bars, 10 μm.) (*E*) Velocities of P-SAW and SAW calculated from the COMSOL eigensolver as a function of the angle between propagation vector *k* and the *y* axis on the z-cut $LiNbO_3$ surface. (*F*) Line profiles in *D*, showing different oscillation periods along *x* direction (red) and *y* direction (blue). The result is consistent with the higher P-SAW velocity along the *x* axis than that along the *y* axis.

the different oscillation periods in the line profiles (Fig. 4*F*). Similar to the double-DW results, these features are different from the standing-wave patterns in quantum corrals (40) in that the adjacent nodes are not spaced by half-λ. The existence of such patterns does not indicate the presence of acoustic resonance (36). In other words, the bright/dark regions in the MIM-Re images are not directly associated with the constructive/destructive interference of acoustic waves underneath the tip. Instead, they mark the tip locations around which the piezoelectric transduction over a distributed region of tens of microns, much wider than the closed domains themselves, is highly effective/ineffective.

Putting our findings in perspective, we have introduced a special type of interferometry by spatial mapping and numerical modeling of the electroacoustic power conversion in ferroelectric materials. The images of microwave dissipation reveal large internal degrees of freedom in piezoelectric and elastic tensors, which are not accessible by measurements of the acoustic displacement fields. For SAW devices, MEMS/NEMS, and phononic crystals, the spatial variation of piezoelectric effect can substantially influence the system performance. The submicron spatial resolution is also desirable to explore the effect of wave scattering, diffraction, and localization on the energy transduction. In all, microwave imaging may emerge as a powerful tool to probe the intimate coupling of electric and strain/stress fields in these systems.

Methods

Sample Preparation. Congruent $LiNbO_3$ wafers from Gooch & Housego PLC (part 99-00042-01) were used in this experiment. There was no intentional doping in the wafers to avoid additional composition-dependent wall structures. The wafers were poled to be a single domain before the fabrication. Standard photolithography was used to form the desired patterns on one side of the sample. A high voltage of 12 kV was applied across the 0.5-mm wafer in the patterned areas, resulting in polarization switching because the electric field exceeds the coercive field of 21 kV/mm. This electrical poling process was performed at the room temperature. The domain inversion flips the sign of odd-rank tensors, such as polarization *P* (first rank) and piezoelectric tensor *e* (third rank), while leaving the even-rank tensors such as permittivity ε (second rank) and elasticity *c* (fourth rank) unaltered. The single and double DWs in Figs. 1 and 3 are very long (>1 mm) and well isolated (>1 mm away) from other patterns. The corral domain structures in Fig. 4 are at least 50 μm away from the nearby patterns, and the interaction between neighboring domains is small.

Microwave Impedance Microscopy. The MIM experiments were performed on an atomic force microscope (AFM) platform (XE-70) from Park Systems. Details of the shielded MIM probe can be found in ref. 12. Custom-built electronics were used for impedance imaging at frequencies ranging from 285 MHz to 6 GHz. Before the measurements, the phase of the reference signal to the mixer is adjusted such that the two channels are aligned to the real (MIM-Re) and imaginary (MIM-Im) parts of the admittance change, i.e., $V_{\text{MIM-Re}} \propto \Delta G \cdot V_0$ and $V_{\text{MIM-Im}} \propto \Delta B \cdot V_0$. The calibration of our 1-GHz MIM electronics shows that an output signal of 1 mV corresponds to an admittance contrast of 0.3 nS. With a tip voltage $V_0 \sim 0.1$ V, the MIM-Re images can be interpreted by a simple conversion factor in that a $V_{\text{MIM-Re}}$ signal of 1 mV represents a transduced power 1/2 $\Delta G V_0^2$ of 1.5 pW.

Numerical Simulation. The numerical simulation was performed by the Structural Mechanics Module in commercial FEA software COMSOL 4.3. The acoustic fields in Figs. 2 and 3 and Figs. S2 and S4 and the dissipated electrical power were simulated by the linear solver. The eigenmodes of SAW and P-SAW in Fig. 4 and Fig. S5 were calculated by the eigensolver.

ACKNOWLEDGMENTS. We thank Z.-X. Shen, S.-W. Cheong, and S. Artyukhin for helpful discussions. The MIM work (L.Z., X.W., Y.-L.H., and K.L.) was supported by NSF Division of Materials Research Award 1707372. The numerical simulation (H.D. and Z.W.) was supported by the Packard Fellowships for Science and Engineering and NSF Division of Engineering Grant EFMA-1641069. The MIM instrumentation was supported by the US Army Research Laboratory and the US Army Research Office under Grant W911NF1410483. W. Wang and W. Wu were supported by US Department of Energy, Office of Science, Basic Energy Sciences, under Award DE-SC0018153.

1. Hariharan P (1992) *Basics of Interferometry* (Academic, San Diego).
2. Clerckx B, Oestges C (2013) *MIMO Wireless Networks: Channels, Techniques and Standards for Multi-Antenna, Multi-User and Multi-Cell Systems* (Academic, Waltham, MA), 2nd Ed.
3. Zheng J (2005) *Optical Frequency-Modulated Continuous-Wave (FMCW) Interferometry* (Springer, New York).
4. Abbott BP, et al.; LIGO Scientific Collaboration and Virgo Collaboration (2016) Observation of gravitational waves from a binary black hole merger. *Phys Rev Lett* 116:061102.
5. Makhlin Y, Schön G, Shnirman A (2001) Quantum-state engineering with Josephson-junction devices. *Rev Mod Phys* 73:357–400.
6. Rosen PA, et al. (2000) Synthetic aperture radar interferometry. *Proc IEEE* 88:333–382.
7. Bushberg JT, Seibert JA (2011) *The Essential Physics of Medical Imaging* (Lippincott Williams & Wilkins, Philadelphia).
8. Weigel R, et al. (2002) Microwave acoustic materials, devices, and applications. *IEEE Trans Microw Theory Tech* 50:738–749.
9. Ekinci KL (2005) Electromechanical transducers at the nanoscale: Actuation and sensing of motion in nanoelectromechanical systems (NEMS). *Small* 1:786–797.
10. Yudistira D, et al. (2014) Monolithic phononic crystals with a surface acoustic band gap from surface phonon-polariton coupling. *Phys Rev Lett* 113:215503.
11. Lai K, Kundhikanjana W, Kelly M, Shen ZX (2010) Nanoscale microwave microscopy using shielded cantilever probes. *Appl Nanosci* 1:13–18.
12. Yang YL, et al. (2012) Batch-fabricated cantilever probes with electrical shielding for nanoscale dielectric and conductivity imaging. *J Micromech Microeng* 22:115040.
13. Lai K, Kundhikanjana W, Kelly M, Shen ZX (2008) Modeling and characterization of a cantilever-based near-field scanning microwave impedance microscope. *Rev Sci Instrum* 79:063703.
14. Wu D, et al. (2015) Thickness-dependent dielectric constant of few-layer In_2Se_3 nanoflakes. *Nano Lett* 15:8136–8140.
15. Wu D, et al. (2016) Uncovering edge states and electrical inhomogeneity in MoS_2 field-effect transistors. *Proc Natl Acad Sci USA* 113:8583–8588.
16. Weis RS, Gaylord TK (1985) Lithium niobate: Summary of physical properties and crystal structure. *Appl Phys A Solids Surf* 37:191–203.
17. Slobodnik AJ, Jr, Carr PH, Budreau AJ (1970) Microwave frequency acoustic surface-wave loss mechanisms on $LiNbO_3$. *J Appl Phys* 41:4380–4387.
18. Yamanouchi K, Shibayama K (1972) Propagation and amplification of Rayleigh waves and piezoelectric leaky surface waves in $LiNbO_3$. *J Appl Phys* 43:856–862.
19. Yamada M, Nada N, Saitoh M, Watanabe K (1993) First-order quasi-phase matched $LiNbO_3$ waveguide periodically poled by applying an external field for efficient blue second-harmonic generation. *Appl Phys Lett* 62:435–436.
20. Liang H, Luo R, He Y, Jiang H, Lin Q (2017) High-quality lithium niobate photonic crystal nanocavities. *Optica* 4:1251–1258.
21. Lu Y, et al. (1999) Optical properties of an ionic-type phononic crystal. *Science* 284:1822–1824.
22. Crommie MF, Lutz CP, Eigler DM (1993) Imaging standing waves in a two-dimensional electron gas. *Nature* 363:524–527.
23. Wu X, et al. (2017) Low-energy structural dynamics of ferroelectric domain walls in hexagonal rare-earth manganites. *Sci Adv* 3:e1602371.
24. Takayanagi A, Yamanouchi K, Shibayama K (1970) Piezoelectric leaky surface wave in $LiNbO_3$. *Appl Phys Lett* 17:225–227.
25. Kushibiki J, Takanaga I, Arakawa M, Sannomiya T (1999) Accurate measurements of the acoustical physical constants of LiNbO (3) and LiTaO(3) single crystals. *IEEE Trans Ultrason Ferroelectr Freq Control* 46:1315–1323.
26. Royer D, Dieulesaint E (1999) *Elastic Waves in Solids* (Springer, New York).
27. Bleustein JL (1968) A new surface wave in piezoelectric materials. *Appl Phys Lett* 13:412–413.
28. Gulyaev YV (1969) Electroacoustic surface waves in piezoelectric materials. *JETP Lett* 9:37–38.
29. White RM (1970) Surface elastic waves. *Proc IEEE* 58:1238–1276.
30. Sugawara Y, et al. (2002) Watching ripples on crystals. *Phys Rev Lett* 88:185504.
31. Profunser DM, Wright OB, Matsuda O (2006) Imaging ripples on phononic crystals reveals acoustic band structure and Bloch harmonics. *Phys Rev Lett* 97:055502.
32. Roshchupkin DV, Fournier T, Brunel M, Plotitsyna OA, Sorokin NG (1992) Scanning electron microscopy observation of excitation of the surface acoustic waves by the regular domain structures in the $LiNbO_3$ crystals. *Appl Phys Lett* 60:2330–2331.
33. Roshchupkin DV, Brunel M (1994) Scanning electron microscopy observation of surface acoustic wave propagation in the $LiNbO_3$ crystals with regular domain structures. *IEEE Trans Ultrason Ferroelectr Freq Control* 41:512–517.
34. Hesjedal T, Behme G (2001) High-resolution imaging of a single circular surface acoustic wave source: Effects of crystal anisotropy. *Appl Phys Lett* 79:1054–1056.
35. Hesjedal T (2010) Surface acoustic wave-assisted scanning probe microscopy–A summary. *Rep Prog Phys* 73:016102.
36. Johnston SR, et al. (2017) Measurement of surface acoustic wave resonances in ferroelectric domains by microwave microscopy. *J Appl Phys* 122:074101.
37. Li J-H, Chen L, Nagarajan V, Ramesh R, Roytburd AL (2004) Finite element modeling of piezoresponse in nanostructured ferroelectric films. *Appl Phys Lett* 84:2626–2628.
38. Kalinin SV, Rar A, Jesse S (2006) A decade of piezoresponse force microscopy: Progress, challenges, and opportunities. *IEEE Trans Ultrason Ferroelectr Freq Control* 53:2226–2252.
39. Tonami S, Nishikata A, Shimizu Y (1995) Characteristics of leaky surface acoustic waves propagating on $LiNbO_3$ and $LiTaO_3$ substrates. *Jpn J Appl Phys* 34:2664–2667.
40. Crommie MF, Lutz CP, Eigler DM (1993) Confinement of electrons to quantum corrals on a metal surface. *Science* 262:218–220.